Supplemental Material: Frequency splitting of chiral phonons from broken time reversal symmetry in CrI$_3$

John Bonini,[1] Shang Ren,[2] David Vanderbilt,[2] Massimiliano Stengel,[3, 4] Cyrus E. Dreyer,[5, 1] and Sinisa Coh[6]

[1]*Center for Computational Quantum Physics, Flatiron Institute,*
162 5th Avenue, New York, New York 10010, USA
[2]*Department of Physics and Astronomy, Rutgers University, Piscataway, New Jersey 08845-0849, USA*
[3]*Institut de Ciència de Materials de Barcelona (ICMAB-CSIC), Campus UAB, 08193 Bellaterra, Spain*
[4]*ICREA-Institució Catalana de Recerca i Estudis Avançats, 08010 Barcelona, Spain*
[5]*Department of Physics and Astronomy, Stony Brook University, Stony Brook, New York, 11794-3800, USA*
[6]*Materials Science and Mechanical Engineering, University of California Riverside, CA 92521, USA*
(Dated: January 20, 2023)

S1. FINITE DIFFERENCE APPROACH FOR CALCULATING BERRY CURVATURES

Here we provide some details of our density-functional theory (DFT) finite-displacement approach for calculating the interatomic force constant (IFC) matrix **C**, and the adiabatic velocity-force coupling **G**. The IFC matrix is calculated in the conventional way [S1, S2] by displacing each nucleus i by distance $\delta\tau = 0.015$ Å in each Cartesian direction, and calculating the resulting forces. The wave functions from these displaced calculations are saved for the following steps. The full velocity-force matrix elements [see Eq. (3) in the main text] are calculated by considering closed paths among these displaced configurations, as discussed in Sec. S1 A, while the matrix elements **G** under the spin-Berry approximation [see main text Eq. (4)] are determined by calculating the canting of the Cr spins from the same displacements, see Sec. S1 B.

A. Velocity-force coupling

Stokes' theorem equates the integral of the Berry curvature over some region in parameter space with the integral of the Berry potential along the boundary of that region. We consider the Berry phase $\phi_{i\alpha,j\beta}$ corresponding to a state evolving adiabatically along a triangular path from the ground state structure to displacement $\tau_{i\alpha}$, then to displacement $\tau_{j\beta}$, and back to the ground state. Assuming $\delta\tau$ is small enough that the Berry curvature is constant over the area of the path,

$$G_{i\alpha,j\beta} = \frac{2\hbar\phi_{i\alpha,j\beta}}{|\ \tau_{i\alpha} \wedge \tau_{j\beta}\ |}, \tag{S1}$$

where $\tau_{i\alpha}$ is a displacement of nucleus i in direction α. Since these displacements are chosen as orthogonal, the wedge product is simply $\delta\tau^2$. For a finite system, letting $\psi(\tau_{i\alpha})$ be the ground state electronic wave function for the displaced structure, we compute the three-point discrete Berry phase

$$\phi_{i\alpha,j\beta} = -\mathrm{Im}\ln\left[\langle\psi(0)\mid\psi(\tau_{i\alpha})\rangle\langle\psi(\tau_{i\alpha})\mid\psi(\tau_{j\beta})\rangle\langle\psi(\tau_{j\beta})\mid\psi(0)\rangle\right], \tag{S2}$$

where $\psi(0)$ indicates the ground state without displacements. For a solid calculated within DFT, Eq. (S2) holds for the single-band case, except that we define $\psi_{\mathbf{k}}(\tau_{i\alpha})$ to be the Kohn-Sham Bloch wavefunctions for the displaced structures, and we must average over k points in the first Brillouin zone. That is,

$$\phi_{i\alpha,j\beta} = -\frac{1}{N_{\mathbf{k}}}\sum_{\mathbf{k}}\mathrm{Im}\ln\left[\langle\psi_{\mathbf{k}}(0)\mid\psi_{\mathbf{k}}(\tau_{i\alpha})\rangle\langle\psi_{\mathbf{k}}(\tau_{i\alpha})\mid\psi_{\mathbf{k}}(\tau_{j\beta})\rangle\langle\psi_{\mathbf{k}}(\tau_{j\beta})\mid\psi_{\mathbf{k}}(0)\rangle\right], \tag{S3}$$

where $\mathbf{k}$ is the Bloch wave vector and $N_{\mathbf{k}}$ is number of k points in the Brillouin zone. The generalization of the discrete Berry phase for multiple bands can be found in Ref. S3, and is given by

$$\phi_{i\alpha,j\beta} = -\frac{1}{N_{\mathbf{k}}}\sum_{\mathbf{k}}\mathrm{Im}\ln\mathrm{Det}[M^k(0,\tau_{i\alpha})M^k(\tau_{i\alpha},\tau_{j\beta})M^k(\tau_{j\beta},0)], \tag{S4}$$

where the overlap matrices are defined as

$$M^k_{mn}(\tau,\tau') = \langle\psi_{mk}(\tau)|\psi_{nk}(\tau')\rangle \tag{S5}$$

with m and n being the band indices.

B. Velocity-force coupling under spin-Berry approximation

To obtain the "spin-Berry approximation" of Eq. (4), we first approximate Eq. (3) as $\bar{G}_{mn} \simeq B_{Ia,m} G_{Ia,Jb} B_{Jb,n}$, where $G_{Ia,Jb} = -2\hbar \operatorname{Im}\langle \partial_{Ia}\psi | \partial_{Jb}\psi \rangle$ is the Berry curvature of the wavefunctions in the parameter space spanned by the Cr spins; $B_{Ia,n} = \partial s_{Ia}/\partial \tilde{u}_n$ is a "spin canting matrix" describing the static change in the equilibrium spin unit vector on magnetic Cr site I in direction a resulting from phonon perturbation n; and $\tilde{u}_n$ is the amplitude of mode n such that the set of atomic displacements are given by $\tilde{u}_n\tilde{\eta}_n$. Here a runs only over x, y directions corresponding to the two possible tilt angles. We have assumed the total magnitude of the spin is unchanged and that tilt angles are small so that $S_{Ix} = S\sin(\theta_{Ix}) \approx Ss_{Ix}$. Under the assumption that the spin Berry curvature dominates, we can further approximate $G_{Ia,Jb} = -S\,\delta_{IJ}\epsilon_{ab}$, where spin $S = 3\hbar/2$ for Cr and ϵ_{ab} is the antisymmetric tensor, yielding Eq. (4) of the main text.

Within the spin-Berry approximation of Eq. (4) in the main text, the matrix elements of $\mathbf{G}$ are obtained from the response of the localized spins to atomic displacements. The assumption is that for a given closed path along which nuclear coordinates are changed, the total Berry phase is given by the sum of the Berry phases picked up by each local spin along that path. Each spin picks up a phase equal to minus the total spin magnitude ($-S = -3/2$, in our case), times the solid angle on the Bloch sphere that is swept out along the path. For small canting angles and with all spins pointing along z in the ground state, $\mathbf{G}$ is then constructed using Eq. (S1) with $\phi_{i\alpha,j\beta}$ now given by

$$\phi_{i\alpha,j\beta} = -\frac{S}{2}\sum_I \left(s_{Ix}(\tau_{i\alpha})s_{Iy}(\tau_{j\beta}) - s_{Iy}(\tau_{i\alpha})s_{Ix}(\tau_{j\beta})\right). \tag{S6}$$

Equivalently, $\mathbf{G}$ could be constructed from the derivatives of the spins with respect to atomic displacements as in Eq. (4) in the main text.

Irrep	$\hbar\tilde{\omega}$ (meV)	s_{1x}	s_{1y}	s_{2x}	s_{2y}
E_g	6.9999	-0.01047	0.00416	-0.01047	0.00416
		-0.00416	-0.01047	-0.00416	-0.01047
	12.9287	-0.00253	-0.01356	-0.00253	-0.01356
		-0.01356	0.00253	-0.01356	0.00253
	13.4876	0.00521	-0.00847	0.00521	-0.00847
		-0.00847	-0.00521	-0.00847	-0.00521
	29.8521	0.00028	-0.00317	0.00028	-0.00317
		0.00317	0.00028	0.00317	0.00028
E_u	10.7667	0.00008	-0.00095	-0.00008	0.00095
		0.00095	0.00008	-0.00095	-0.00008
	14.3259	0.00101	0.00142	-0.00101	-0.00142
		0.00142	-0.00101	-0.00142	0.00101
	27.8168	0.00251	-0.00057	-0.00251	0.00057
		-0.00057	-0.00251	0.00057	0.00251

TABLE SI. Derivative of spin canting of Cr atoms 1 and 2 in Cartesian directions x and y with respect to amplitudes of E_g and E_u modes in ferromagnetic CrI$_3$. The units for the spin derivatives with respect to mode amplitude are $\sqrt{\mathrm{meV}}/\hbar$. Degenerate mode pairs are labeled by their unperturbed frequencies $\hbar\tilde{\omega}$; the two rows for each entry correspond to the two modes comprising the pair in a real basis.

S2. CONTRIBUTION OF SPIN CANTING TO ADIABATIC VELOCITY-FORCE COUPLING

In Table SII we compare the velocity-force coupling computed under the Mead-Truhlar (MT) approach (i.e., assuming adiabatic electron dynamics), using the $\mathbf{G}$ matrix obtained from the the full wave function Berry curvature as in Eq. (3) of the main text (labeled "W"), with the $\mathbf{G}$ matrix obtained from the spin-Berry approximation of Eq. (4) of the main text (labeled "S"). Modes are labeled by their irrep and frequency as determined only from the IFC matrix ($\tilde{\omega}$). For each pair we show the magnitude of the matrix element between the degenerate modes (G_{ij}) and frequency splitting $\Delta\omega$. Deviations between matrix elements and frequency splitting occur only when $\mathbf{G}$ induces mixing between the degenerate subspaces. We see that indeed, the spin-Berry contribution accounts for the majority of velocity-force coupling. For the three lowest-frequency E_g modes and the E_u mode near 14 meV, the agreement is excellent, within 1%. For the highest-frequency E_g mode and the other two E_u modes, the spin-Berry contribution has a discrepancy of 25-43%. This indicates that other terms, such as the "phonon-only Berry curvature" resulting

from atomic displacements at fixed spins, may have a significant contribution. In any case, within the MT theory, the splittings of the highest-frequency E_g mode and all of the E_u modes are quite small, so the error in absolute terms is not large.

Irrep	$\hbar\tilde{\omega}$ (meV)	MT (W)		MT (S)	
		$\hbar\bar{G}_{ij}$ (meV)	$\hbar\Delta\omega$ (meV)	$\hbar\bar{G}_{ij}$ (meV)	$\hbar\Delta\omega$ (meV)
E_g	6.9999	0.3825	0.3820	0.3808	0.3803
	12.9287	0.5685	0.5270	0.5712	0.5293
	13.4876	0.2948	0.3368	0.2968	0.3391
	29.8521	0.0243	0.0244	0.0305	0.0306
E_u	10.7667	0.0043	0.0043	0.0027	0.0027
	14.3259	0.0090	0.0090	0.0091	0.0091
	27.8168	0.0349	0.0349	0.0199	0.0199

TABLE SII. Comparison of velocity-force matrix elements ($\bar{G}_{ij} = \eta_i^\dagger \mathbf{G} \eta_j$) and frequency splitting ($\Delta\omega$) of E_u and E_g zone center phonon modes in CrI_3 computed with Berry curvatures obtained from wavefunction overlaps (W) and with Berry curvatures obtained by the solid angle swept out by magnetic moments on the Cr sites (S). Modes are labelled by their irrep and frequency determined only from the interatomic force constants ($\hbar\tilde{\omega}$).

S3. FREQUENCIES OF ALL MODES

In the spin-phonon model (SP) of Eq. (5) the γ parameter is related to the magnitude of the $\bar{\mathbf{G}}$ matrix elements coupling degenerate modes i and j by $\gamma = \omega_m\sqrt{S\bar{G}_{ij}}$. Here the natural choice for the $\bar{G}_{ij}$ value from which to obtain γ is that of the spin-Berry approximation, as γ is really defined in terms of spin-phonon coupling. We use experimental magnon frequencies of 0.3 (acoustic) and 17 meV (optical), from Ref. [S4]. We note that other magnon frequencies for CrI_3 are reported in the literature [S5]. In our model, choosing a different value simply corresponds to changing ω_m in Eq. (6). Though this does not change the qualitative conclusions, it may have a quantitative effect, since the energy difference between a given degenerate phonon mode and the magnon it couples to is a significant factor in the magnitude of the splitting (c.f., Fig. 2). It is in general possible for a system to have a nonzero MT term even when evaluated at fixed spin, as well as a distinct γ coupling to spin degrees of freedom; this will be explored in subsequent work. While the SP values presented here incorporate nonadiabatic effects not present in the nuclear MT theory, they do not include any coupling of modes outside the degenerate subspace (that is, there is no mixing between modes with distinct $\tilde{\omega}$).

In order to present the effects of these different levels of approximation independently, we consider four possible $\mathbf{G}$ matrices for MT (labeled W, w, S, and s) and two possible $\mathbf{G}$ matrices for SP (w and s). As above, W and S correspond to $\mathbf{G}$ matrices obtained using Eq. (3) and Eq. (4) of the main text, respectively. Results labeled "w" and "s" correspond to setting all couplings between nondegenerate $\tilde{\omega}$ equal to zero in "W" and "S" $\mathbf{G}$ matrices respectively. In Table SIII we give the frequencies of all of the optical modes (including the singly-degenerate ones), from the IFC matrix only ($\hbar\tilde{\omega}$), with adiabatic Mead-Truhlar (MT), and in the spin-phonon model (SP), for each of these cases.

S4. ANGULAR MOMENTUM OF CHIRAL PHONONS

In the main text we discussed the fact that including TRS breaking via $\mathbf{G}$ in the equations of motion resulted in chiral phonons with well-defined angular momenta. From the symmetry of CrI_3, specifically the three-fold rotation axis in the out-of-plane z direction, the total angular momentum of a normal mode can only have z components. For mode n, the angular momentum is found via $l_z^{(n)} = 2\hbar\sum_j m_j \mathrm{Im}[\eta_n^*(jx)\eta_n(jy)]$[S6, S7], where j runs over the atomic sublattices and m_j is the mass of nucleus j. If we neglect $\mathbf{G}$ in Eq. (2), then the angular momentum of modes in a degenerate subspace spanned by ($\tilde{\eta}_1, \tilde{\eta}_2$) depends on the basis we choose. Clearly, l_z vanishes in the real basis $\tilde{\eta}_n$ introduced above, while a complex "circularly polarized" combination of degenerate modes of the form $\eta'_\pm = \tilde{\eta}_1 \pm i\tilde{\eta}_2$ will have equal and opposite l_z (since we are at the Γ point [S8]), with the magnitude determined by the mode displacement patterns. Neglecting terms in the $\bar{\mathbf{G}}$ matrix that mix different degenerate subspaces, the chiral modes after splitting will have exactly the eigendisplacements $\eta'_\pm$. Such mixing is neglected in the spin-phonon model of Eq. (6), where we are working in the context of a model that couples a single pair of degenerate phonons with the magnon degrees of freedom. At this level, the phonon parts of the eigenvectors are also identical with their uncoupled (circularly polarized) counterparts, so that the nuclear angular momentum is unchanged.
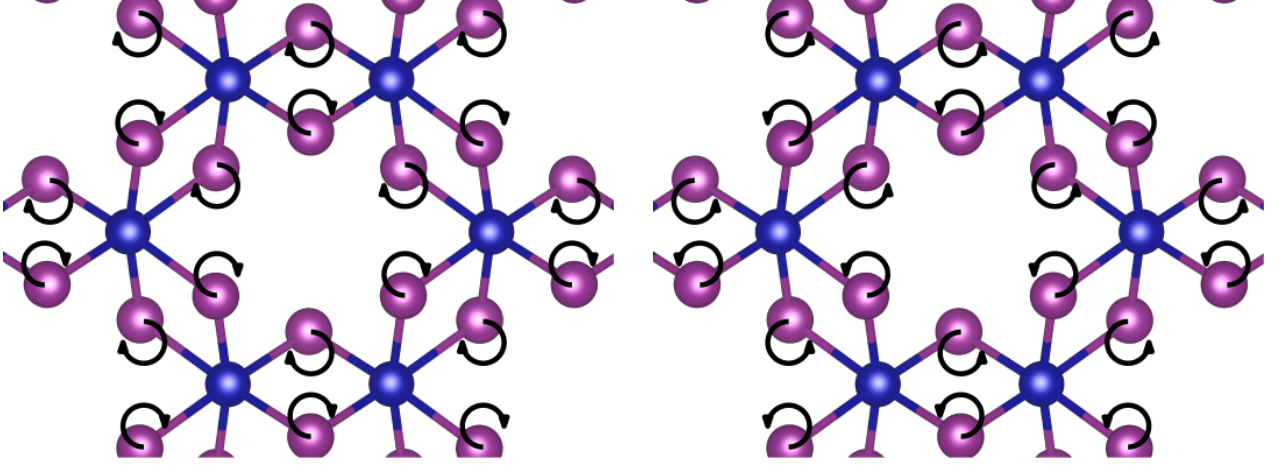
FIG. S1. Schematic of chiral trajectories of selected zone-center phonon modes in a single layer of bulk CrI$_3$. In the presence of time-reversal symmetry breaking, such phonons occur at distinct frequencies.

Consider, for example, the green E_g mode in Fig. 1(b) of the main text with unperturbed frequency $\hbar\tilde{\omega} = 13.5$ meV. The angular momentum of this mode mode is due to the in-plane motion of iodine atoms. Choosing the two degenerate modes $\tilde{\eta}_x$ and $\tilde{\eta}_y$ to involve real displacements of I atoms moving in the x and y directions respectively, neither of these modes has a non-zero angular momentum by itself. However, the complex circularly polarized combination $\eta'_\pm = (\tilde{\eta}_x \pm i\tilde{\eta}_y)/\sqrt{2}$, which corresponds to the circular displacement patterns shown in Fig. S1 clearly has a finite l_z. In Fig. 1(c) of the main text, we plot the angular momentum of the modes after including the velocity-force coupling, with the color corresponding to the mode on the right side of Fig. 1(b). For the E_g modes near 13 meV [green and orange in Fig. 1(b)] an analysis of the displacement patterns and angular momentum of the split modes is complicated by the fact that all four modes can mix [unlike the higher-frequency split mode and the gray E_u mode above it in Fig. 1(b)]. Thus the angular momentum contributions seen in Fig. 1(c) are mixed between these modes.

A large velocity-force coupling does not necessarily result in a large phonon angular momenta after splitting,

$\hbar\tilde{\omega}$	MT (W)	MT (w)	SP (w)	MT (S)	MT (s)	SP (s)
6.9999	6.8021	6.8113	6.9996	6.8030	6.8122	6.9996
6.9999	7.1841	7.1938	7.0003	7.1832	7.1929	7.0003
8.1265	8.1265	8.1265	8.1265	8.1265	8.1265	8.1265
9.9535	9.9535	9.9535	9.9535	9.9535	9.9535	9.9535
10.7667	10.7645	10.7645	10.7575	10.7653	10.7653	10.7608
10.7667	10.7688	10.7688	10.7646	10.7680	10.7680	10.7653
11.3471	11.3471	11.3471	11.3471	11.3471	11.3471	11.3471
12.9287	12.6100	12.6475	12.9285	12.6082	12.6462	12.9285
12.9287	13.1369	13.2161	12.9288	13.1375	13.2174	12.9288
13.4876	13.3989	13.3410	13.4875	13.3983	13.3400	13.4875
13.4876	13.7357	13.6358	13.4877	13.7374	13.6368	13.4877
14.3259	14.3214	14.3214	14.2924	14.3213	14.3213	14.2919
14.3259	14.3304	14.3304	14.3230	14.3305	14.3305	14.3230
16.5013	16.5013	16.5013	16.5013	16.5013	16.5013	16.5013
16.6023	16.6023	16.6023	16.6023	16.6023	16.6023	16.6023
26.5081	26.5081	26.5081	26.5081	26.5081	26.5081	26.5081
27.8168	27.7993	27.7993	27.8127	27.8068	27.8068	27.8145
27.8168	27.8342	27.8342	27.8335	27.8267	27.8267	27.8263
29.8521	29.8407	29.8400	29.8521	29.8376	29.8369	29.8521
29.8521	29.8650	29.8643	29.8521	29.8681	29.8674	29.8521
31.7361	31.7361	31.7361	31.7361	31.7361	31.7361	31.7361

TABLE SIII. Frequencies in meV of optical phonon modes of ferromagnetic CrI$_3$ at the zone-center computed with different levels of theory. $\hbar\tilde{\omega}$ labels frequencies computed using only the force constant matrix. MT refers to frequencies computed within the adiabatic velocity-force, or Mead-Truhlar formalism. SP refers to frequencies computed in the spin-phonon model. Labels W, w, S, and s refer to different couplings used in each calculation as explained in Sec. S3.

as seen for the case the lowest two E_g modes [blue curves in Fig. 1(b) of the main text]. The relatively modest angular momentum of these modes [see Fig. 1(c) of the main text] is a result of the fact that the motions of the real eigendisplacements before the inclusion of the $\mathbf{G}$ perturbation involve *out-of-plane* motions of I atoms, not just in-plane motions like those depicted in Fig. S1. This is allowed by symmetry since individual atoms may have in-plane angular momentum components l_x and l_y, as long as these components sum to zero over all atoms. The resulting l_z is then significantly reduced compared to the green 13.5 meV E_g mode. Similar considerations apply to other modes; thus the out-of-plane components in the eigenvectors of the E_g (and E_u) modes directly lead to a lower magnitude of the total mode angular momentum. Note that even though the blue E_g mode is quite isolated in frequency compared to the other E_g modes, the asymmetry of l_z of the modes after splitting indicates significant mixing with these other modes.

Finally, we can see in Fig. 1(c) of the main text that higher frequency modes tend to have higher angular momentum. This is likely due to the fact that the in-plane vibrations in CrI$_3$ tend to have higher frequency, and, as pointed out above, only in-plane displacements contribute to l_z.

S5. COMPUTATIONAL DETAILS

We perform calculations on CrI$_3$ in the ferromagnetic ground state using the VASP code [S9–S11], the local density approximation exchange-correlation functional [S12], and projector-augmented wave potentials [S13]. Semicore ($3s$, $3p$) and ($5s$, $5p$) states are included in the valence for Cr and I respectively. A $5 \times 5 \times 5$ Monkhorst-Pack grid [S14] is used to sample the Brillouin zone, and the energy cutoff for the plane-wave basis set is 520 eV. Spin-orbit coupling, which is essential to the physics described here, is included in all calculations.

The canting of spins at localized atomic sites induced by lattice perturbations are utilized by both the spin-Berry approximation for the adiabatic velocity-force coupling [Eq. (4) in the main text] and the non-adiabatic spin-phonon model [Eq. (5) in the main text]. We use the procedure implemented in VASP to obtain local magnetic moments by integrating the magnetization inside a sphere centered on each Cr site. The spin canting values used to parameterize Eqs. (4) and (5) are approximated as the differences in these local magnetic moments. We set a sphere radius of 1.165Å, the recommended value specified in the VASP pseudopotential for Cr.

Since the velocity-force terms are dominated by canting of *local* magnetic moments the results are not significantly impacted by k-mesh sampling. In Table SIV we demonstrate this by comparing the frequency splittings of two representative modes (both in the spin-phonon and MT approach) for k-meshes of $5 \times 5 \times 5$, $7 \times 7 \times 7$, and $9 \times 9 \times 9$. Note that small deviation from these $5 \times 5 \times 5$ results and those presented in Table I of the main text is due to the fact that the k-mesh convergence test was done with a less strict criteria for convergence of the magnetic moment direction in order to make it computationally tractable.

S6. SPIN PHONON MODEL

An effective spin-phonon model was presented in Eq. (5) of the main text with equations of motion given in Eq. (6). The coupling between spin and phonon degrees of freedom is given as $\gamma = \partial^2 E / \partial x \partial s_x$. Here we have made use of the freedom in basis choice for the two degenerate phonon modes to simplify the presentation. Any 2×2 unitary rotation on the eigenvectors of the modes leaves their frequencies unchanged; in Eq. (5) of the main text this basis was chosen such that the eigenvectors are real and the xs_y and ys_x terms vanish. Note that due to C_3 symmetry

$\hbar\omega$ (meV)	6.9999 (E_g)		14.3259 (E_u)	
theory	MT	SP	MT	SP
$5 \times 5 \times 5$	3.779×10^{-1}	6.918×10^{-4}	8.328×10^{-3}	2.912×10^{-2}
$7 \times 7 \times 7$	3.779×10^{-1}	6.911×10^{-4}	8.321×10^{-3}	2.886×10^{-2}
$9 \times 9 \times 9$	3.777×10^{-1}	6.912×10^{-4}	8.273×10^{-3}	2.880×10^{-2}

TABLE SIV. Comparison of splitting for a single E_g and E_u mode with different k-mesh samplings of $5 \times 5 \times 5$, $7 \times 7 \times 7$, and $9 \times 9 \times 9$. Results are presented with both the Mead-Truhlar (MT) approach and the spin-phonon (SP) model.

$\partial^2 E/\partial x \partial s_x = \partial^2 E/\partial y \partial s_y$ in any basis where the phonon eigenvectors are real.

$$H = \frac{1}{2}(p_x^2 + p_y^2) + \frac{1}{2}\tilde{\omega}^2(x^2 + y^2)$$
$$+ \frac{1}{2}\alpha(s_x^2 + s_y^2) + \gamma(xs_x + ys_y). \tag{S7}$$

Semi-classical equations of motion for this coupled spin-phonon Hamiltonian can be obtained from the time dependence of the expectation values of the spin and phonon coordinates in the Heisenberg picture, or equivalently by treating Eq. (5) as a classical Hamiltonian with the appropriate Poisson brackets for the spin degrees of freedom [S15]. The time dependence of an operator $\mathcal{O}$ expectation value in the Heisenberg picture of a Hamiltonian with no time dependence is given by is given by $\frac{d}{dt}\langle\mathcal{O}\rangle = \frac{i}{\hbar}[H,\mathcal{O}]$; in the following semi-classical approach we will drop the $\langle\ldots\rangle$. Utilizing the commutators

$$[x, p_x] = i\hbar \qquad\qquad [y, p_y] = i\hbar \qquad\qquad [s_x, s_y] = i\hbar S^{-1}s_z \tag{S8}$$

we take $s_z \approx 1$ since we are considering small tilts of the spins from their ground state. Carrying out the commutation relations to find the time derivative of the expectation value for each x, y, p_x, p_y, s_x, s_y and moving to circularly polarized coordinates defined as

$$x_\pm = x \pm iy \qquad\qquad p_\pm = p_x \pm ip_y \qquad\qquad s_\pm = s_x \pm is_y \tag{S9}$$

the following equations of motion are obtained

$$\dot{x}_\pm = p_\pm$$
$$\dot{p}_\pm = -\tilde{\omega}^2 x_\pm - \gamma s_\pm \tag{S10}$$
$$\dot{s}_\pm = \mp i\omega_{\mathrm{m}}s_\pm \mp iS^{-1}\gamma x_\pm$$

where $\omega_{\mathrm{m}} = \alpha/S$. Examining solutions where $d/dt\mathcal{O} = -i\omega\langle\mathcal{O}\rangle$ the above equations reduce to Eq. (6) from the main text.

In the adiabatic MT approach the strong coupling between E_g phonon modes is dominated by the spin-Berry term associated with unrealistically large induced tilts of the spins. In the non-adiabatic theory, we have represented the dynamic spin tilts explicitly, and neglected any direct interaction between phonon modes of different frequency. To understand this approximation, we can consider treating the magnon-phonon interaction as a perturbation. Letting each pair of unperturbed degenerate phonon modes be expressed in a "circularly polarized" basis, each mode will couple directly to magnon states leading to a frequency splitting that is quadratic in the spin-phonon coupling. Interactions between phonon modes of different frequencies occur indirectly through the magnon channel, so that their contributions to the mode splitting come in only at fourth order in the coupling. Thus, we expect mixing between phonon modes of different frequency to have little impact on the splittings in the non-adiabatic theory. While we expect such mixing to be small, it can be accounted for by treating simultaneously the interaction of all phonon modes with the magnons. A more general treatment of the problem that explicitly includes these and other effects will be the topic of a future publication.

[S1] Xavier Gonze and Changyol Lee, "Dynamical matrices, Born effective charges, dielectric permittivity tensors, and interatomic force constants from density-functional perturbation theory," Phys. Rev. B **55**, 10355–10368 (1997).

[S2] Stefano Baroni, Stefano de Gironcoli, Andrea Dal Corso, and Paolo Giannozzi, "Phonons and related crystal properties from density-functional perturbation theory," Reviews of Modern Physics **73**, 515–562 (2001).

[S3] David Vanderbilt, *Berry Phases in Electronic Structure Theory: Electric Polarization, Orbital Magnetization and Topological Insulators* (Cambridge University Press, 2018) Chap. 3.

[S4] John Cenker, Bevin Huang, Nishchay Suri, Pearl Thijssen, Aaron Miller, Tiancheng Song, Takashi Taniguchi, Kenji Watanabe, Michael A. McGuire, Di Xiao, and Xiaodong Xu, "Direct observation of two-dimensional magnons in atomically thin CrI$_3$," Nature Physics **17**, 20–25 (2021).

[S5] Wencan Jin, Hyun Ho Kim, Zhipeng Ye, Siwen Li, Pouyan Rezaie, Fabian Diaz, Saad Siddiq, Eric Wauer, Bowen Yang, Chenghe Li, *et al.*, "Raman fingerprint of two terahertz spin wave branches in a two-dimensional honeycomb ising ferromagnet," Nature communications **9**, 1–7 (2018).

[S6] Lifa Zhang and Qian Niu, "Angular momentum of phonons and the Einstein–de Haas effect," Phys. Rev. Lett. **112**, 085503 (2014).

[S7] A G McLellan, "Angular momentum states for phonons and a rotationally invariant development of lattice dynamics," Journal of Physics C: Solid State Physics **21**, 1177–1190 (1988).

[S8] Sinisa Coh, "Classification of materials with phonon angular momentum and microscopic origin of angular momentum," (2019), arXiv:1911.05064 [cond-mat.mtrl-sci].

[S9] G. Kresse and J. Hafner, "Ab initio molecular dynamics for liquid metals," Phys. Rev. B **47**, 558–561 (1993).

[S10] G. Kresse and J. Furthmüller, "Efficient iterative schemes for ab initio total-energy calculations using a plane-wave basis set," Phys. Rev. B **54**, 11169–11186 (1996).

[S11] G. Kresse and D. Joubert, "From ultrasoft pseudopotentials to the projector augmented-wave method," Phys. Rev. B **59**, 1758–1775 (1999).

[S12] J. P. Perdew and Alex Zunger, "Self-interaction correction to density-functional approximations for many-electron systems," Phys. Rev. B **23**, 5048–5079 (1981).

[S13] P. E. Blöchl, "Projector augmented-wave method," Phys. Rev. B **50**, 17953–17979 (1994).

[S14] Hendrik J. Monkhorst and James D. Pack, "Special points for Brillouin-zone integrations," Phys. Rev. B **13**, 5188–5192 (1976).

[S15] Th.W. Ruijgrok and H. Van der Vlist, "On the hamiltonian and lagrangian formulation of classical dynamics for particles with spin," Physica A: Statistical Mechanics and its Applications **101**, 571–580 (1980).